Earth Planets Space, **63**, 391–396, 2011

Global modeling of hot O distribution in the upper thermosphere

F. S. Bessarab and Yu. N. Korenkov

Western Department of IZMIRAN, Kaliningrad, 236017, Russia

(Received June 4, 2010; Revised December 28, 2010; Accepted January 25, 2011; Online published June 14, 2011)

The existence of hot oxygen (hot O, O_h) in the upper thermosphere is mainly confirmed by optical observations of high-altitude airglow. In the experiments described here, a peak of O_h population was found at an altitude of approximately 550 km with a temperature of about 4000 K. Although it was shown that O_h concentration could reach a value of 1–2% with respect to ambient (cold) O, a realistic global distribution of O_h concentration and temperature has not been established. The presence of non-thermal atoms in the thermosphere leads to variations in the thermo-dynamical regime in the upper atmosphere. The major chemical processes involved in O_h production were taken into account in the time-dependent, Global Self-consistent Model of Thermosphere, Ionosphere and Protonosphere (GSM TIP) of the Earth in order to simulate global distribution of O_h concentration and temperature (T_h). Calculations were carried out in the geomagnetic coordinate system for moderate solar, quiet geomagnetic conditions, and winter season. It was shown that the maximum O_h is located at -60° latitude, 300° longitude, and 24 UT. The T_h maximum is about 2050 K. This temperature and O_h concentration cause an increase in neutral gas temperature at high thermosphere by ∼100 K during daytime and by ∼70 K during nighttime. Variations in the neutral gas velocity circulation were calculated. The maximum increase in neutral velocity was about 36 m/s, corresponding to $\Phi = 50^\circ$, $\Lambda = 180^\circ$ in the northern and $\Phi = -50^\circ$, $\Lambda = 270^\circ$ in the southern hemisphere.

Key words: Global modeling of the upper atmosphere, photochemical processes, hot oxygen.

1. Introduction

Experimental evidence for the existence of hot oxygen (hot O, O_h) in thermosphere was first presented by Yee *et al.* (1980) who inferred a population of O_h atoms from twilight measurements of O^+ emission at 732 nm. At an altitude of 550 km and temperature of ≥4000 K, the number density reaches 10^5–10^6 cm^{-3}. Further experimental evidence was supplied by Hedin (1989), who estimated O_h densities to be equal to $(1–3) \cdot 10^5$ cm^{-3} at an altitude of 550 km based on differences between MSIS model and satellite drag models. The high-resolution rocket data on atomic oxygen dayglow emissions at altitudes ranging from 150 to 960 km was obtained by Cotton *et al.* (1993a). These researchers reported that the modeled 130.4-nm and 98.9-nm emission lines underestimated the measured intensities of oxygen. Analyses of radar data have shown that a heat source is needed to explain the detected ion temperature (Oliver, 1997): the calculated O_h concentration was insufficient to account for the observed excess EUV emission.

Cotton *et al.* (1993b) subsequently reanalyzed the data incorporating the effects of O_h. A comparison of the new results with those obtained from the standard model of a neutral atmosphere shows that the O_h geocorona has an intensity peak as high as 10^6 cm^{-3} at 550 km, with the temperature of O_h being 4000 K.

A large amount of O_h is created as a result of photochemical processes. The importance of chemical sources for O_h geocorona has been discussed in detail by Gerard *et al.* (1995). The most complete list of the chemical reactions for O_h is given in papers by Richards *et al.* (1994) and Hickey *et al.* (1995).

Modeling of the O_h concentration is rather complicated procedure, and researchers very often adopt a diffusive equilibrium for the altitude profile of the O_h concentration. Various procedures have been adopted in attempts to obtain an altitude profile of O_h concentration. In the stochastic calculations of the oxygen energy distribution function (EDF) described by Shematovich *et al.* (1994), a non-thermal oxygen concentration of ∼1% with respect to cold O content was obtained with a characteristic hot temperature of ∼4000 K. In the study of Shoendorf *et al.* (2000), O_h profiles were obtained using mass and energy equations methods, and the ionosphere parameters (T_i, T_e, N_e) were taken from International Reference Ionosphere (IRI) (Bilitza, 2001). However, these authors were used a simplified method of deriving O_h profiles and the variation in O_h temperature with changing altitude.

The loss processes of hot atoms are governed by thermalization. These processes include translational energy or velocity relaxation through collisions with molecules and atoms of ambient gases and ions. Inelastic collisions may also occur in which the kinetic energy of atoms is transferred to the rotational and vibrational motion of the ambient gas molecules. Obviously, the presence of oxygen atoms with energies exceeding the thermal energy of ambient oxygen in the exospheric altitudes would lead to a change in the thermodynamic regime of the upper thermo-

doi:10.5047/eps.2011.01.009

Table 1. Sources of hot oxygen (O_h).

	Reaction	Rate ($cm^3\ s^{-1}$)	O_h heating (eV)
1.	$N(^2D) + O \rightarrow O_h + N(^4S)$	$7 \cdot 10^{-13}$	1.11
2.	$N(^2D) + O^+ \rightarrow O_h + N(^4S)$	$5 \cdot 10^{-11}$	0.68
3.	$N(^2D) + O_2 \rightarrow O_h + NO$	$6 \cdot 10^{-12}$	2.45
4.	$N(^2D) + NO \rightarrow O_h + N_2$	$7 \cdot 10^{-11}$	3.58
5.	$N_2^v + O \rightarrow O_h + N_2$	$1.7 \cdot 10^{-10} \cdot \exp(-69.9 \cdot T^{-1/3})$	0.19
6.	$NO^+ + e \rightarrow N(^2D) + O_h$	$4.3 \cdot 10^{-7}(300/T_e)$ (78%)	0.18
7.	$NO^+ + e \rightarrow N(^4S) + O_h$	$4.3 \cdot 10^{-7}(300/T_e)$ (22%)	1.28
8.	$O_2^+ + e \rightarrow O + O_h$	$1.6 \cdot 10^{-7}(300/T_e)^{0.55}$ (33%)	3.48
9.	$O_2^+ + e \rightarrow O(^1D) + O_h$	$1.6 \cdot 10^{-7}(300/T_e)^{0.55}$ (21%)	2.51
10.	$O_2 + O^+ \rightarrow O_2^+ + O_h$	$2.1 \cdot 10^{-11}$	1.03

sphere. It should be noted that this problem has as yet not been properly considered.

In the study reported here, we used the Global Self-consistent Model of the Thermosphere, Ionosphere and Protonosphere (GSM TIP) of the Earth to carry out numerical calculations of O_h density and temperature on the global scale. We also studied the effect of O_h on temperature and circulation of the neutral gas.

Model calculations were executed for the winter solstice, moderate solar activity, and quiet geomagnetic conditions. Global distributions of O_h concentration and temperature were obtained by solving corresponding equations numerically using the appropriate technique.

2. Brief GSM TIP Description

The Global Self-consistent Model of the Thermosphere, Ionosphere and Protonosphere was developed in the West Department of IZMIRAN of the Russian Academy of Sciences and simulates the time-dependent global structure of the near-Earth space environment from 80 km to 15 Earth radii.

In the thermospheric block of the model, global distribution of the neutral gas temperature (T_n) and of N_2, O_2, O, NO, $N(^4S)$, and $N(^2D)$ concentration, as well as the three-dimensional circulation of the neutral gas and N_2^+, O_2^+, and NO^+, and also their temperature (T_i) and velocities (V_i), are calculated in the range from 80 to 520 km in the spherical geomagnetic coordinate system. In the vertical dimension, the thermospheric code uses 30 layers, with each layer approximately equal to a thickness of one scale height.

In the ionospheric section of the model, global time-dependent distributions of ions, electron temperatures (T_i, T_e), vector velocity (V_i), and O^+ and H^+ ion concentrations are calculated in the magnetic dipole coordinate system from 175 km in the northern hemisphere to 175 km in the southern hemisphere. In this case, the ionosphere code for atomic ions does not require the upper boundary condition. The convection patterns imposed by the magnetospheric electric field on plasma movements in the polar region are referenced to a fixed Sun-Earth frame, assuming pure $E \times B$ drifts. The electric field is derived from calculation of the two-dimensional distribution of the electric field potential of dynamo and magnetospheric origin. The solution of the full system of equations of the model is performed numerically on a global grid with resolutions of 5° in latitude and 15° in longitude as specified in the spherical geomagnetic coordinate system; the time step is 2 min.

Model inputs are the solar EUV and UV spectra (10–1760 Å). The precipitating electron fluxes and distribution of the field-aligned currents in the first- and second high-latitude region are specified in the solar-magnetic frame. The transformations between all coordinate systems in the model are given by standard formulas.

In our model, the first region of the field-aligned currents (FACs) is located at ±75° magnetic latitude, while the location of the second region of the FACs is at ±65°. The values of FACs were adjusted so that the polar cup potential difference was in agreement with the statistical model of Oliver *et al.* (1983) for the quiet geomagnetic conditions ($K_p \sim 2$). For the solar EUV flux, we have used the technique of Nusinov (1984) to construct the flux spectra for the period under study. For the electron precipitations, we mark out several precipitation zones. At both hemispheres, we have an auroral oval electron flux precipitation with a characteristic energy of 3 keV and a maximal flux of ~4 erg/(cm^2 s) at 00 MLT (Magnetic Local Time). Further, we have the soft electron flux in the cusp region of 0.2 keV, an energy flux of 0.2 erg/(cm^2 s) and the diffusive precipitation in the nighttime sector with 0.1 keV electrons, an energy flux of ~0.1 erg/(cm^2 s). The spectral characteristic of the soft and energetic precipitating electrons was chosen according to the Maxwellian energy distribution. The spatial distribution has Gaussian form in both the longitudinal and latitudinal directions. The adopted auroral precipitating energy flux and spatial distribution are typical for lower geomagnetic conditions and in accordance with the statistical model of Hardy *et al.* (1985).

The model has been described in detail by Namgaladze *et al.* (1988, 1990, 1991), and its application has been presented in the papers by Korenkov *et al.* (1996, 1998, 2003, 2009).

3. Hot Oxygen Model Equations

Two three-dimensional equations for O_h describe mass and energy conservation:

$$\frac{\partial n_h}{\partial t} + \mathrm{div} \perp (n_h \mathbf{V}) + \frac{\partial \Phi}{\partial r} = q_h - l_h \quad (1)$$

$$\frac{3}{2} k n_h \frac{dT_h}{dt} + P_h \mathrm{div}\mathbf{V} - \mathrm{div}(\lambda\ \mathrm{grad}\, T_h) = Q - L \quad (2)$$

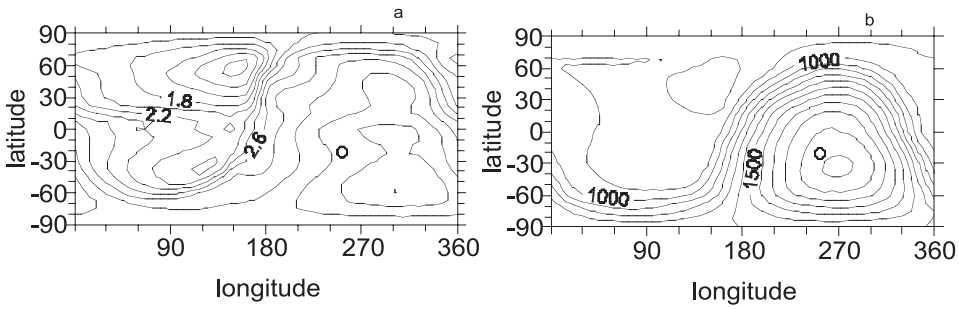

Fig. 1. Contour plot of the logarithm of O_h density (a) and temperature (b) at 500 km for 24 UT. The position of the subsolar point is marked with a circle.

Where T_h, n_h are the temperature and density of the O_h, **V** is a vector of average mass velocity, q_h, l_h represent the sources and losses of O_h, Φ is a vertical flux due to diffusion, P_h is a pressure, λ is a conductivity for O_h, Q and L are O_h thermal energy sources and losses, and k is Boltzmann's constant. The molecular diffusion coefficient for O_h differs from that of ambient oxygen and is calculated in accordance with the concepts of diffusion for a two-temperature mixture of gases (Ivanovsky *et al*., 1967).

From the 27 possible sources of O_h in the thermosphere that are presently known (Hickey *et al*., 1995), we take into account only main reactions. The list of the adopted reaction is presented in Table 1.

All components of the chemical reactions listed in Table 1, except for the concentration of vibrationally excited nitrogen (N_2^v), are modeled in the GSM TIP. The N_2^v concentration and temperature were adopted as reported in the paper by Korenkov *et al*. (1996):

$$N_2^v = N_2\left(1 - \exp\left(-\frac{3353}{T_v}\right)\right) \cdot \exp\left(-\frac{i \cdot 3353}{T_v}\right), \quad (3)$$

where T_v is the temperature of N_2^v, and i is the vibrational levels from 1 to 2. The temperature of the vibrationally excited nitrogen was approximated by $a \cdot T_e$, where a is a coefficient ranging from 1.1 to 1.3 in our calculations.

The losses of O_h occurs in collisions with cold atoms and molecular and ions of O^+:

$$l_h = n_h\left(\upsilon_{O_h-O^+} + \upsilon_{O_h-O} + \upsilon_{O_h-N_2}\right), \quad (4)$$

where $\upsilon_{O_h-O^+}$, υ_{O_h-O}, $\upsilon_{O_h-N_2}$ are the collision frequencies between O_h and O^+, cold O, and N_2, respectively.

Represent collisions are accompanied with heat transfer from O_h to cold neutral species and ions:

$$L = \frac{3}{2} n_h \cdot k \cdot \left(\upsilon_{O_h-O^+} \cdot (T_h - T_i) + \upsilon_{O_h-O} \cdot (T_h - T_n) + \upsilon_{O_h-N_2} \cdot (T_h - T_n)\right), \quad (5)$$

where T_i, T_n are the temperatures of the ion and cold neutral gas, respectively.

The boundary conditions for the O_h mass equation are chemical equilibrium at lower boundary and diffusion equilibrium at upper boundary. For the energy equation at lower boundary we put $T_h = T_n$ (cold), while at upper boundary we adopt $dT_h/dr = 0$. The time step was chosen to be 2 min. The model equations were integrated until the solution reaches the quasi-stationary regime.

Input parameters are based on accumulated experimental data and represent average values for the geophysical condition under study. Input data cannot vary within wide limits for the given conditions.

4. Results

Results of model calculations are presented in Figs. 1–3 in the geomagnetic Cartesian coordinate system for 24 UT for various values of T_v and, accordingly, N_2^v. Several variants of the calculations were carried out, which are different in approximations for T_v. The main results were obtained at $T_v = 1.1 \cdot T_e$, where T_e is electron temperature. Figures 1–3 correspond to that very case, unless specifically indicated otherwise.

Figure 1 shows the logarithm of the global distribution of O_h concentrations (cm^{-3}) (Fig. 1(a)) and of temperature (K) of O_h (Fig. 1(b)) at 500 km. From the global distribution of O_h concentration, it can be seen that the maximum of $\lg(n_h)$ is about 3.5 and located at -60° latitude and 285° longitude at these altitudes. The maximum O_h temperature is about 2050 K at the same altitude and located at -40° latitude and 270° longitude. Both maxima are detected in the southern-summer hemisphere. Global minima of the O_h concentration and temperature are located in the northern-winter hemisphere. Note here that maximum of O_h density does not coincide in space with the temperature maximum.

The altitude profiles of the O_h temperature and density corresponding to three model runs for various T_v values at the points of global temperature maximum and minimum are presented in Fig. 2(a) and (b), respectively. Solid lines correspond to the main version of calculations ($T_v = 1.1 \cdot T_e$), while dashed and dash-dotted lines correspond to $T_v = 1.2 \cdot T_e$ and $T_v = 1.3 \cdot T_e$, respectively.

As can be seen from Fig. 2, the temperature profiles of O_h are similar to the standard temperature profile of neutral gas in, for example, the MSIS or IRI models because the thermal conductivity of O_h concentration is large enough to smooth any significant concentration profile variations. The temperature of O_h at daytime conditions is about twofold that of the standard temperature of neutral gas and may be as high as 2000 K (the main version of calculations), possibly even reaching a value of 3900 K for a model run with $T_v = 1.3 \cdot T_e$.

The altitude profiles of n_h have pronounced maxima at al-

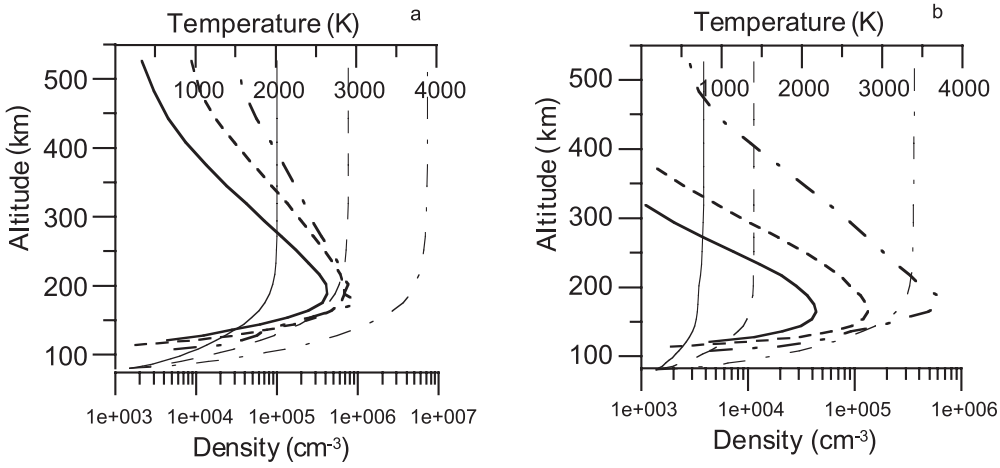

Fig. 2. The altitude profiles of the O_h temperature (thin lines) and density (thick lines) corresponding to three model runs at points of global temperature daytime maximum (a) and nighttime minimum (b). Solid lines correspond to $T_v = 1.1 \cdot T_e$, dashed and dash-dotted lines correspond to $T_v = 1.2 \cdot T_e$, $T_v = 1.3 \cdot T_e$ respectively.

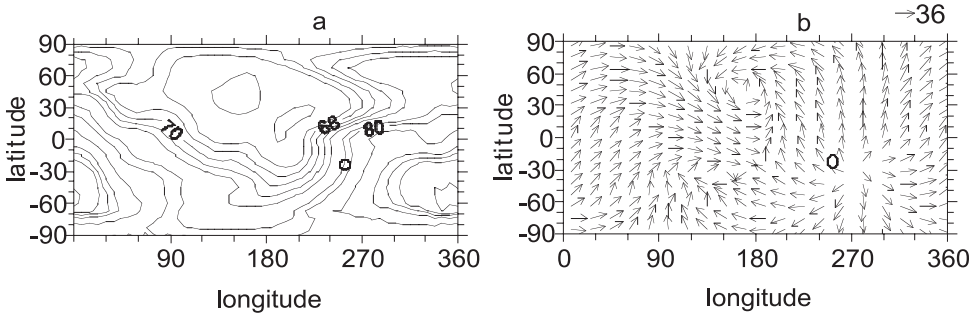

Fig. 3. Increase in neutral temperature (a) and changes in dynamical regime (b) due to hot oxygen heating at 500 km.

titudes of <200 km. A daytime maximum for the main version of calculations is located at about 180 km and reaches a value of $4 \cdot 10^5$ cm^{-3}. A nighttime maximum is located at about 160 km and is as high as $4 \cdot 10^4$ cm^{-3}. These maxima are due to chemical reactions in the lower thermosphere and diffusive equilibrium at the higher altitudes.

This temperature and O_h concentration increase the neutral gas temperature in the high thermosphere and modify the neutral gas circulation. T_h spatial distribution of gain at the neutral temperature due to O_h heating is presented in Fig. 3(a) where T_n can be seen to increase by ∼100 K during the daytime and by ∼65 K during the nighttime.

Figure 3(b) illustrates the variability of the dynamical regime at ionosphere altitudes on a global scale. The distribution of neutral gas velocity gain due to taking into account O_h and normal circulation (without O_h) is shown in Fig. 3(b). The maximum increase in neutral gas velocity is about 36 m/s and corresponds to $\Phi = 50^\circ$, $\lambda = 180^\circ$ in the northern and $\Phi = -50^\circ$, $\Lambda = 270^\circ$ in the southern hemisphere at an altitude of 500 km.

5. Discussion

As was mentioned above, O_h attracts attention because of discrepancies between experimental data (mostly from observations of O emissions) and theoretical estimates of ambient O near the exobase and above.

Most estimates give values for the effective O_h temperature that fall in a range of 4000–6000 K. In terms of its concentration, O_h is estimated to be present at between about 0.1% and 1% relative to the cold O content at an altitude of 400 km (Shematovich *et al.*, 1994; Oliver, 1997; Litvin and Oliver, 2000).

The major part of the experimental data present here was obtained under the assumption that T_i and UV airglow intensity calculated from theory were significantly lower than those measured. This discrepancy could be reduced by including an additional heat source, for example, O_h.

Although qualitative estimates of O_h absolute density as a function of altitude do exist, a definitive density profile shape has not yet been established. At present, it is assumed that O_h is more likely to form a layer (Cotton *et al.*, 1993a; Schoendorf *et al.*, 2000) than a concentration profile which decreases with altitude (Shematovich *et al.*, 1994).

However, in practical calculations, a diffusive equilibrium density profile is used with a reference density of 0.1–1% at an altitude of 400 km (Alcayde *et al.*, 2001; Zettergren *et al.*, 2006) with T_h 4000–5000 K. These altitude profiles of the O_h population are taken in order to fit the experimental data. However, they do not have much physical basis.

Figure 4 illustrates some samples of the O_h density profile that have been presented by other authors

As can be seen from Fig. 4, the dispersion of experimental estimates of O_h concentration at 400–500 km is very

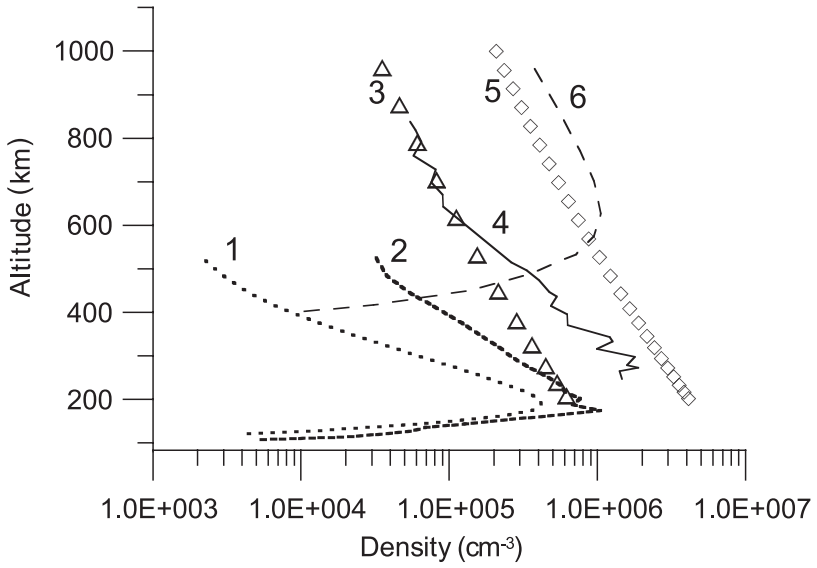

Fig. 4. The altitude profiles of O_h density: 1, 2, GSM TIP simulation (see text); 3, Alcayde *et al*. (2001); 4, Shematovich *et al*. (1994); 5, Zettergren *et al*. (2006); 6, Hubert and Gerard (1999).

large.

The calculation results within our model are also presented Fig. 4. However, one can directly compare model values and experimental estimates only at altitudes within the indicated range, where measurements of the appropriate parameters are carried out.

We obtained a density profile of O_h with a peak located at about 200 km, reaching the value of about $4 \cdot 10^5$ cm^{-3}. These results do not agree with experimental data. Therefore, the model calculations show that the density of O_h at 400 km is about 10^4 cm^{-3} or 0.001% of the cold O concentration, while the experimental estimates give 0.1% with respect to cold O content. The temperature of O_h is about 2000 K in the GSM TIP model calculations, which is somewhat less than the universally adopted value. There could be several explanations for these discrepancies.

Firstly, our model does not take into consideration some of the chemical reactions mentioned in the paper by Hickey *et al*. (1995). Most of these reactions involve metastable species, for example, O(^{1}D), O(^{1}S), and electron exited ions, such as $O^+(^2D)$ and $O^+(^2P)$. The importance of these reactions lies in that they allow the electronic energy transfer to another species at the higher altitudes. However, Hickey *et al*. (1995) and Richards *et al*. (1994) studies these reactions, although they did not present the altitude profiles of the density and temperature of O_h. Another reason for the low O_h concentration and temperature in the model calculations could be the choice of inappropriate boundary conditions, in which the flux of O_h and energy are not included. These fluxes arise from ion-neutral reactions in the plasmasphere. Bisikalo *et al*. (1995) proposed energetic O^+ ions precipitation to be a possible source of high-latitude O_h concentration, and hence the boundary conditions must be based on O_h temperature and density values found in the experimental data and literature. Another important point in terms of the model calculations is the choice of the temperature of the vibrationally excited N_2 because this component plays an important role in the chemistry and energetics of the ionosphere (Richards and Torr, 1986; Korenkov *et al*., 1996). As can be seen from Fig. 2, a large T_v value produces a significant variation in O_h density and temperature. We note here that the vibrational temperature is substantially higher than the neutral temperature and a little less than the electron temperature (Richards and Torr, 1986). However, the exact value of the T_v has not yet been reliably established.

The GSM TIP model can simulate the global distributions of all thermosphere/ionosphere parameters. In this study, we present global distributions for the temperature and concentration of O_h and their effect on the thermospheric temperature and global circulation of neutral gas. As can be seen from Figs. 1 and 2, both maxima of T_h and O_h are formed during the daytime, although Oliver and Schoendorf (1999) pointed out that O_h density at an altitude of 400 km is the lowest during the day and highest at nighttime. However, this assumption is scarcely relevant since all of the sources of O_h are regulated by the sun.

Increases in T_n (Fig. 3(a)) cause pressure disturbances in the upper thermosphere and, consequently, variations in the neutral gas velocity (Fig. 3(b)). It is noted here that the largest corrections to T_n took place in the evening sector, 90 K at $\Phi = -60^\circ$ and $\Lambda = 360^\circ$ and 36 m/s in the latitudinal component of a vector neutral gas in the night sector.

Thus, our simulations of global distribution of O_h density and temperature within the GSM TIP model show that even a small fraction of O_h has a significant impact on the thermo-dynamical structure of the upper atmosphere. On the other hand, the issue of the self-consistent modeling of O_h remains unsolved and requires further study.

6. Conclusion

We have presented calculation results on the spatiotemporal distribution of O_h concentration and temperature on the global scale. These results were obtained using GSM TIP model.

The results of this study indicate that the O_h density profile has layer shape, with a peak located at about 200 km altitude.

Our calculations show that a small fraction of O_h (<0.5% with respect to cold oxygen content) had a significant impact on the heat budget and dynamical regime of the neutral gas. Hot O causes an increase in neutral gas temperature up to 100 K at daytime and up to 65 K at nighttime. The vector velocity value rises to 36 m/s.

Our calculations also show that reactions with vibrationally exited N_2 are very important for the production of O_h.

A number of problems, such as chemical processes, boundary conditions, and others, need to be solved.

These results may be used in the analysis of the energy and dynamical regimes of the Earth's upper atmosphere.

Acknowledgments. The authors thank the referees for critical reading manuscript and helpful comments.

References

Alcayde, D., P.-I. Blelly, W. Kofman, A. Litvin, and W. I. Oliver, Effects of hot oxygen in the ionosphere: TRANSCAR simulations, *Ann. Geophys.*, **19**, 257–261, 2001.

Bilitza, D., International Reference Ionosphere 2000, *Radio Sci.*, **36**, 261–275, 2001.

Bisikalo, D. V., V. I. Shematovich, and J. C. Gerard, A kinetic model of the formation of the hot oxygen geocorona, 2. Influence of O^+ ion precipitation, *J. Geophys. Res.*, **100**, 3715–3720, 1995.

Cotton, D. M., G. R. Gladstone, and S. Chakrabarti, Sounding rocket observation of a hot atomic oxygen geocorona, *J. Geophys. Res.*, **98**, 21651–21657, 1993a.

Cotton, D. M., S. Chakrabarti, and G. R. Gladstone, Preliminary results from the Berkeley EUV airglow rocket spectrometer: O I and N_2 FUV/EUV dayglow in the thermosphere and lower exosphere, *J. Geophys. Res.*, **98**, 21627–21641, 1993b.

Gerard, J. C., P. G. Richards, V. I. Shematovich, and D. V. Bisikalo, The importance of new chemical sources for the oxygen geocorona, *Geophys. Res. Lett.*, **22**, 279–282, 1995.

Hardy, D. A., J. Gussenhoven, and D. Brautigam, A statistical model of auroral electron precipitation, *J. Geophys. Res.*, **90**, 4229–4248, 1985.

Hedin, A. E., Hot oxygen geocorona as inferred from neural exospheric models and mass spectrometer measurements, *J. Geophys. Res.*, **94**, 5523–5529, 1989.

Hickey, M. P., P. G. Richards, and D. G. Torr, New sources for the hot oxygen geocorona: Solar cycle, seasonal, latitudinal and diurnal variations, *J. Geophys. Res.*, **100**, 17377–17388, 1995.

Hubert, B. and J.-C. Gerard, Effect of hot oxygen on the thermospheric O I UV airglow, *J. Geophys. Res.*, **104**, 17139–13143, 1999.

Ivanovsky, A. I., A. I. Repnev, and E. Shvidlovsky, *Kinetic Theory of The Upper Atmosphere*, Leningrad, Gidrometeorizdat press, 1–258, 1967 (in Russian).

Korenkov, Yu. N., V. V. Klimenko, M. Forster, V. A. Surotkin, and J. Cmilauer, Global modeling study (GSM TIP) of the ionospheric effects of excited N_2, convection and heat fluxes by comparison with EISCAT and satellite data for 31 July 1990, *Ann. Geophys.*, **14**, 1362–1374, 1996.

Korenkov, Yu. N., V. V. Klimenko, M. Forster, F. S. Bessarab, and V. A. Surotkin, Calculated and observed ionospheric parameters for Magion-2 passage above EISCAT on July 31 1990, *J. Geophys. Res.*, **103**, 14697–14710, 1998.

Korenkov, Yu. N., V. V. Klimenko, and F. S. Bessarab, Model/Data comparison of the F2-regions parameters for the August 11, 1999 Solar Eclipse, *Adv. Space. Res.*, **31**, 995–1000, 2003.

Korenkov, Yu. N., V. V. Klimenko, and F. S. Bessarab, Global comparison of the model results of GSM TIP with IRI for summer conditions, *Adv. Space Res.*, **43**, 1633–1637, 2009.

Litvin, A. and W. L. Oliver, Hot O and nighttime ionospheric temperatures, *Geophys. Res. Lett.*, **27**, 2821–2824, 2000.

Namgaladze, A. A., Yu. N. Korenkov, V. V. Klimenko, I. V. Karpov, F. S. Bessarab, V. A. Surotkin, T. A. Glushenko, and N. M. Naumova, Global model of the thermosphere-ionosphere-protonosphere system, *Pure Appl. Geophys.*, **127**, 219–254, 1988.

Namgaladze, A. A., Yu. N. Korenkov, V. V. Klimenko, I. V. Karpov, F. S. Bessarab, V. A. Surotkin, T. A. Glushenko, and N. M. Naumova, A global numerical model of the thermosphere, ionosphere and protonosphere of the Earth, *Geomag. Aeron.*, **30**, 515–521, 1990 (in Russian).

Namgaladze, A. A., Yu. N. Korenkov, V. V. Klimenko, I. V. Karpov, V. A. Surotkin, and N. M. Naumova, Numerical modeling of the thermosphere-ionosphere-protonosphere system, *J. Atmos. Terr. Phys.*, **53**, 1113–1124, 1991.

Nusinov, A. A., Dependence of intensity of lines of shortwave radiation of the Sun on activity level, *Geomag. Aeron.*, **24**, 529–536, 1984 (in Russian).

Oliver, W. L., Hot oxygen and the ion energy budget, *J. Geophys. Res.*, **102**, 2503–2511, 1997.

Oliver, W. L. and J. Schoendorf, Variations of hot O in the thermosphere, *Geophys. Res. Lett.*, **26**, 2829–2832, 1999.

Oliver, W. L., J. M. Holt, R. H. Wand, and J. V. Evans, Millstone Hill incoherent scatter observation of auroral convection over $60^\circ \leq \Lambda \leq 75^\circ$. 3. Average patterns versus Kp, *J. Geophys. Res.*, **88**, 5505–5516, 1983.

Richards, P. G. and D. G. Torr, A factor of 2 reduction in theoretical F2 peak electron density due to enhanced vibrational exitation of N_2 in summer a Solar maximum, *J. Geophys. Res.*, **91**, 11331–11336, 1986.

Richards, P. G., M. P. Hickey, and D. G. Torr, New sources for the hot oxygen geocorona, *Geophys. Res. Lett.*, **22**, 279–282, 1994.

Shematovich, V. I., D. V. Bisikalo, and J. C. Gerard, A kinetic model of the formation of the hot oxygen geocorona, 1, Quiet geomagnetic conditions, *J. Geophys. Res.*, **99**, 23217–23228, 1994.

Shoendorf, J., L. A. Young, and W. L. Oliver, Hot oxygen profiles for incoherent scatter radar analysis of ion energy balance, *J. Geophys. Res.*, **105**, 12823–12832, 2000.

Yee, J. H., J. W. Meriwether, and P. B. Hayes, Detection of a corona of fast oxygen atoms during solar maximum, *J. Geophys. Res.*, **85**, 3396–3400, 1980.

Zettergren, M. D., W. L. Oliver, P.-l. Blelly, and D. Alcayde, Modeling the behavior of hot oxygen ions, *Ann. Geophys.*, **24**, 1625–1637, 2006.

F. S. Bessarab (e-mail: pcizmiran@gazinter.net) and Yu. N. Korenkov